Electron Density and Its Relation with Electronic and Optical Properties in 2D Mo/W Dichalcogenides

Pingping Jiang, Marie-Christine Record, P. Boulet

nanomaterials

MDPI

Article

Electron Density and Its Relation with Electronic and Optical Properties in 2D Mo/W Dichalcogenides

Pingping Jiang [1], Marie-Christine Record [2,*] and Pascal Boulet [1]

[1] Aix-Marseille University, UFR Sciences, CNRS, MADIREL, 13013 Marseille, France; pingping.jiang@etu.univ-amu.fr (P.J.); pascal.boulet@univ-amu.fr (P.B.)
[2] Aix-Marseille University, UFR Sciences, University of Toulon, CNRS, IM2NP, 13013 Marseille, France
* Correspondence: m-c.record@univ-amu.fr

Received: 8 October 2020; Accepted: 6 November 2020; Published: 8 November 2020

Abstract: Two-dimensional MX_2 (M = Mo, W; X = S, Se, Te) homo- and heterostructures have attracted extensive attention in electronics and optoelectronics due to their unique structures and properties. In this work, the layer-dependent electronic and optical properties have been studied by varying layer thickness and stacking order. Based on the quantum theory of atoms in molecules, topological analyses on interatomic interactions of layered MX_2 and WX_2/MoX_2, including bond degree (BD), bond length (BL), and bond angle (BA), have been detailed to probe structure-property relationships. Results show that M-X and X-X bonds are strengthened and weakened in layered MX_2 compared to the counterparts in bulks. X-X and M-Se/Te are weakened at compressive strain while strengthened at tensile strain and are more responsive to the former than the latter. Discordant BD variation of individual parts of WX_2/MoX_2 accounts for exclusively distributed electrons and holes, yielding type-II band offsets. X-X BL correlates positively to binding energy (E_b), while X-X BA correlates negatively to lattice mismatch (lm). The resulting interlayer distance limitation evidences constraint-free lattice of vdW structure. Finally, the connection between microscopic interatomic interaction and macroscopic electromagnetic behavior has been quantified firstly by a cubic equation relating to weighted BD summation and static dielectric constant.

Keywords: two-dimensional materials; DFT calculations; QTAIM; vdW homo- and hetero-structures; structure-properties relationships

1. Introduction

Ever since the discovery of isolated graphene through mechanical exfoliation [1], other graphene-like and two-dimensional (2D) materials, especially transition metal dichalcogenides (TMDs), have attracted significant research interest, in great part due to their unique structure-property relationships. The versatile applications of TMDs have been demonstrated in different fields, such as electronics, optoelectronics, energy storage and photocatalysis [2–5], despite ongoing challenges in device design and fabrication techniques [6]. Their typical honeycomb-like lattice structures consisting of single or few atomic layers are fundamental for their physical and chemical properties [7]. A wide range of polymorphs and stacking polytypes of TMDs have been defined by the composition, lattice configuration and dimensionality [4]. Among them, the group VI TMDs with formula MX_2 (M = Mo, W; X = S, Se, Te) stand out thanks to their favorable light-matter interaction, carrier mobility and external radiative efficiency [8–12]. Indeed, the phase stability, electronic structure, and semiconducting property strongly depend on the filling state of M-d orbitals [4,13,14]. As such, the covalent intralayer M-X bonds are the main focus of existing studies [15,16]. However, the interlayer X-X bonds have weak van der Waals (vdW) in nature due to the chemically saturated X atoms, are seldom examined

despite being the prime reason for creating atomically thin materials through chemical or mechanical exfoliation [17].

By definition, the layered MX_2 is divided into three polymorphs, the 1T, 2H, and 3R phases, where letters designate a trigonal, hexagonal, or rhombohedral phase and numbers give the repeating unit of the X-M-X motif [18]. The dissimilar electronic behaviors between phases, particularly at the interface, have driven lots of researches on their layer-dependent properties via experimental and theoretical methods. Mono- and few-layered MX_2 are strongly distorted, which affects the stability to a certain extent [4,19]. Eda et al. [20] found the immunity of chemically exfoliated MoS_2 monolayer to structural distortion and local pressure, even though the 1T and 2H phases coexist and form a coherent interface. Additionally, the mechanical strength is linearly dependent on the charge transfer from M to X despite their strong covalent bonding [15]. Huang et al. [16] found that the M-X bond strength plays a key role in phonon propagation, as a result of the competition between ionicity and covalency. Cheng et al. [21] observed a thickness-dependent phase transition and optical behavior of MoS_2 film when hydrostatic pressure is applied. With layer thinning, the blue shift of the bandgap and photoluminescence (PL) have been detected due to the quantum confinement in a layered d-electron system, presenting a tunable band transition [22–25]. Moreover, a weak contribution of interlayer interaction to the valence band splitting of bulk WS_2 was found by Latzke et al. [26].

Sequence stacking two different MX_2 monolayers by vdW forces in either vertical or lateral directions [27,28] offers supplementary degrees of freedom for heterostructure modulation, thus introducing unexpected properties that are beyond those of individual constitutents [28–30]. Heterointerface state has strong implication for predicting physicochemical properties [31]. For instance, the lack of dangling bonds and inactive lone-pair electron at layer-terminated surfaces, and the free of lattice constraint at interfaces help to keep the layer stability against external conditions, irrespective of stacking order [4,32,33]. Previously, substrate, strain, electric field, doping, and defect engineering have been performed on 2D MX_2 [34–37]. Su et al. [38] found that stronger bonding between MoS_2 and substrate results in weaker photoluminescence intensity. Additionally, after subsequent gold nanoparticles deposition, the resulting stress would undermine the Mo-S bonding, thus destabilizing the MoS_2 film [33].

To date, the majority of studies have focused on the structural, electronic, and optical properties of MX_2 with or without strain [14,39–41], whereas our understanding of the electron density features of 2D homo- and heterostructures with vdW binding forces lags far behind, not to mention the strain- and layout-correlated electrostatic interactions in sublayers. Likewise, the possible relationship between optical properties and electron density features of vdW structures has never been studied, to the best of our knowledge. The role of vdW interactions in ionic and semiconductor solids has been extensively discussed both qualitatively and quantitatively [42,43]. A straightforward supposition is to assume a minor effect of vdW force on the overall cohesive properties in solids [44]. However, the correctness and universality in applying this intuition to 2D and bulk TMDs materials are debatable, since the vdW interaction plays a key role in their band structure evolution [26,45]. Thorough investigations are needed. In the quantum theory of atoms in molecules (QTAIM) [46], the distribution of electron density and the interatomic interaction (defined as bond degree [47]), are correlated to single and group atomic contributions to molecular polarizability. Additionally, the frequency-dependent polarizability per crystal unit cell is a summation of all individual constituents [44,48] and related to the dielectric constant, as expressed in the Clausius-Mossotti relation [49]. Since the macroscopic electromagnetic response and the microscopic chemical bond nature are linked by relative permittivity [50], it is safe to presume that individual bond degree contributions would influence the total dielectric function, as expressed by the dielectric constant as a bulk parameter.

Until now, the common-X [28,30,51] and different-X [40,52,53] heterostructures have been widely studied, but the assembly of two MX_2 monolayers with different sublayer M and varying X, totaling nine heterostructures, has not been yet considered. Since the full image of interlayer bonds in multi- and hetero-layers and the evolution of electrostatic interactions with composition and dimensionality

remain unknown, probing the contribution of both interlayer and intralayer bonds in a wide range of structures is of great interest for further understanding of the structure-property relationships of 2D vdW materials. In this work, three major objectives were addressed by DFT and QTAIM: (i) determination of electronic-dependent structural, optical and bonding properties of MX_2-based homo- and heterostructures where M = Mo, W and X = S, Se, Te; (ii) detailing and comparing the effect of layer thickness, stacking schemes and lattice mismatch on interatomic interactions, bond lengths and bond angles; and (iii) understanding the lattice mismatch effect on the vdW structures as well as the electron excitations and charge carriers displacements in the materials.

2. Computational Details

DFT calculations were carried out by a full-potential linear augmented plane wave method (FP-LAPW) as implemented in the program WIEN2k [54]. To precisely characterize the exchange-correlation energy, the WC-generalized gradient approximation (GGA) functional [55], the modified Becke–Johnson exchange potential (mBJ) functional [56] and the van der Waals corrected optB88-vdW functional [42] were applied and compared. During the lattice optimization and relaxation, the convergence criteria of total energy and force on each atom were set to 10^{-5} Ry and 1 mRy/Bohr, respectively. The $R_{mt}K_{max}$ parameter has been set to 7. Additionally, the first Brillouin zone was sampled with a mesh of 1500 ***k***-points using Monkhorst-Pack grids [57]. The lattice constants *a* and *c* and bandgaps of hexagonal $P6_3/mmc$ MoX_2 and WX_2 (X = S, Se, Te) were calculated using WC-GGA and optB88-vdW functionals, and compared with other experimental and theoretical data, as summarized in Table S1. Lattice constants calculated by WC-GGA functional fit better to experimental ones than those calculated by optB88-vdW functional despite the underestimated bandgaps. By using mBJ functional, bandgaps have been improved and agree well with experimental ones due to the accurate semi-local atomic exchange potential [56]. Our parameter settings have been validated and will be used in the following calculations.

The mono, bi-, and trilayered $[MX_2]_n$ slabs in the form of $4 \times 4 \times 1$ supercells were built as layer thickness *n* goes from one to three, respectively. In the meantime, the nine WX_2/MoX_2 heterostructures were modeled by vertically stacking WX_2 and MoX_2 monolayers. Considering boundary conditions and lattice coherence, the in-plane lattice constants of WX_2/MoX_2 were set to the average values of those of bulk MoX_2 and WX_2 to minimize the effect of lattice mismatch, since their elastic properties in monolayers are similar, such as Young's modulus in [15,58]. A 20 Å thickness of vacuum has been added atop to separate free surfaces, avoiding interaction between periodic images. The $10 \times 10 \times 1$ ***k***-meshes were used in the supercell cases. Structure relaxation was performed by using WC-GGA and optB88-vdW functionals until the force on each atom converged to 1 mRy/Bohr. Based on the electron density (ρ) obtained from WIEN2k, the topological properties of ρ for each modeled structure were investigated with the program CRITIC2 [59]. In the QTAIM, the real space is partitioned into atomic basins, and each basin has only one nucleus which is surrounded by the surface of zero-flux electron density ($\Delta\rho = 0$). By applying boundary conditions, the local total (H), kinetic (G), and potential (V) energy density can be obtained by integrating over each atomic basin. For more details about the QTAIM method refer to our previous works [60,61].

3. 2D Multilayers

3.1. Stability, Electronic, and Optical Properties

Figure 1a shows the atomic configurations of mono-, bi- and trilayered $[MX_2]_n$ supercells. Their stabilities are examined by the formation energy E_{form}, which is given by:

$$E_{form} = E_{slab} - \sum_{x = M,X} N_x E_x^{bulk}, \quad (1)$$

where E_{slab} is the total energy of the considered slab and N_x, E_x^{bulk} are the number and bulk energy of atoms involved in the slab, respectively. Interlayer distances between metal (M) and chalcogen (X) atoms from the adjacent X-M-X units, i.e., ③ M′-X and ⑥ M″-X′ in Figure 1a, have been compared with the counterparts in bulks. Their differences $\Delta d_{n,bulk}$ and the above yielded E_{form} are gathered in Figure 1b. All layered and bulk MX_2 are stable at zero Kelvin because of their negative E_{form}. In the meantime, the negative $\Delta d_{n,bulk}$ indicates a reinforced binding strength between adjacent layers in $[MX_2]_n$ compared to those in bulks. Since the bilayer and bulk structure have similar unit cells (two layers of X-M-X unit), the gap between their E_{form} would tell the relative stability. Hence, the WTe_2 bilayer is seen as the least stable, which corresponds to its smallest $\Delta d_{n,bulk}$.

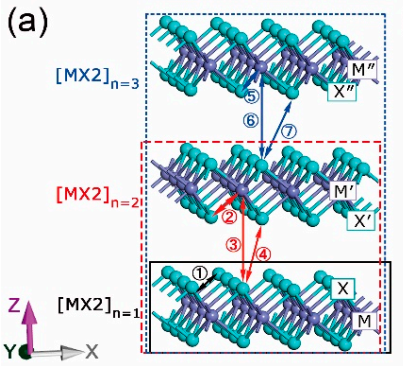

(b)

$[MX_2]_n$	E_{form} (eV/motif)				③	⑥
	n=1	n=2	n=3	bulk	$\Delta d_{2,bulk}$	$\Delta d_{3,bulk}$
MoS_2	-4.40	-8.61	-12.92	-8.70	-1.21	-1.21
$MoSe_2$	-2.51	-5.07	-7.62	-4.99	-1.17	-1.18
$MoTe_2$	-1.20	-2.49	-3.82	-2.53	-0.78	-0.73
WS_2	-4.28	-8.63	-12.90	-8.67	-0.92	-0.92
WSe_2	-2.25	-4.63	-6.96	-4.44	-0.94	-0.71
WTe_2	-0.49	-0.89	-1.00	-1.17	-0.47	-0.42

Figure 1. Scheme of $[MX_2]_n$ supercells with M = Mo, W and X = S, Se, Te when n equals to 1, 2, and 3 (**a**). Metal and chalcogen atoms in the first, second and third X-M-X units are marked as [M, X], [M′, X′], and [M″, X″], respectively. Formation energy E_{form} of bulk and $[MX_2]_n$ slabs and differences of M-X distances in slabs and bulks, $\Delta d_{n,bulk}$ (**b**).

The mutual compromise between bandgap and absorption, which govern voltage and photocurrent, respectively [2], underlines the significance of adjusting bandgap and, hence, absorption startup through layer thickness modification. By adding a vacuum layer atop of layered structures, the uneven interactions of atoms near to and away from the surface will cause physical and chemical deviations from the relevant bulk cases that have intrinsic symmetrical interactions. Thus, apart from the structure stability, further investigations on electronic properties are indispensable. Band structures along the Γ-Σ-M-K-Λ-Γ direction in the first Brillouin zone are plotted in Figures S1 and S2 (Supplemental Files). Along with the most possible transition directions, interband energy gaps are obtained, as seen in Figure 2a,b. With the growth of thickness, transition energy at K-K′ direction changes slowly whereas those at K-Λ and Γ-Λ directions decrease rapidly, yielding a direct bandgap for monolayer and indirect ones for bilayers and trilayers. This holds for MoX_2 and WX_2 materials, except for the direct bandgap of MoS_2 bilayer, which is consistent with the results in [22,58,62]. It is found that the layered and bulk WX_2 have higher and lower bandgap than MoX_2, respectively. In particular, the Γ-Λ transition prevails in bi- and trilayered MoS_2, WS_2, and $MoTe_2$, while the K-Λ transition dominates for the remaining cases, such that the valence band maximum (VBM) and conduction band minimum (CBM) can be determined. The refractive index and absorption coefficient of $[MoS_2]_n$ (as an example) are shown in Figure 3a,b. The photovoltaic (PV) effect grows with the absorber thickness, and that of bulk MoS_2 is the highest. In the *xx* direction, the starting point of photon-electron transformation is earlier than that in the *zz* direction with both experiencing a red-shift peak at ~2.2 eV and 4.4 eV, respectively. Moreover, the refractive indices in the xx direction are higher than those in the *zz* direction, whereas the absorption coefficients behave oppositely.

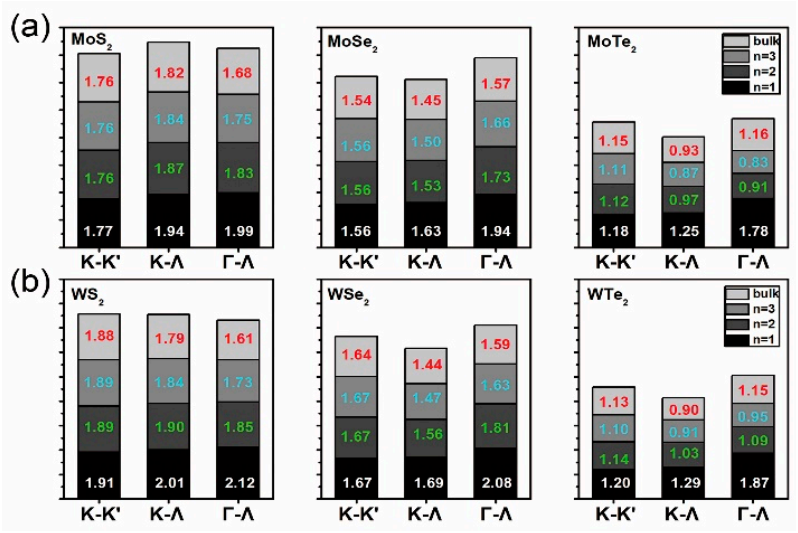

Figure 2. Direct (K-K′) and indirect (K-Λ and Γ-Λ) band transition energy in eV of bulk (red texts), mono- (white texts), bi- (green texts), and trilayered (cyan texts) MoX_2 (**a**) and WX_2 (**b**).

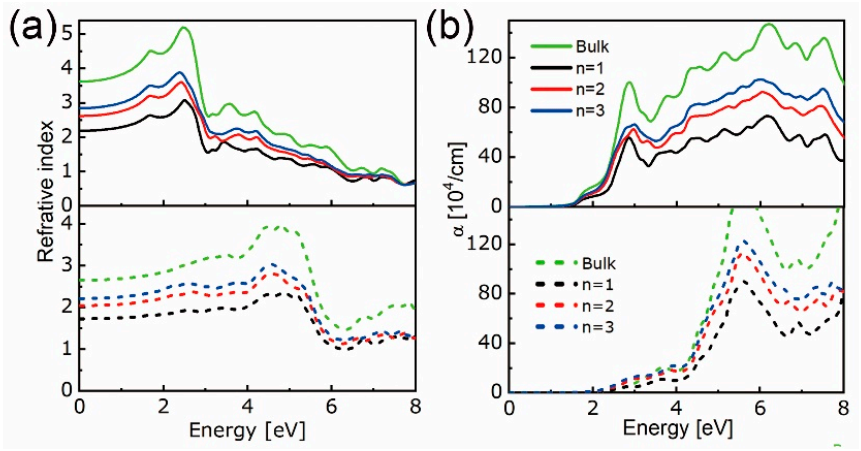

Figure 3. Refractive index (**a**) and absorption coefficient α (**b**) of bulk and layered $[MoS_2]_n$ in the in-plane (top panel) and out-of-plane (bottom panel) directions.

3.2. Electron Density Analysis

Figure S3 (Supplemental Files) displays the distribution of electron density $\rho$and its Laplacian $\nabla^2\rho$of bulk, mono-, bi- and trilayered MoS_2, which is used as an example for visualization. The labels "b", "r", and "c" represent the bond, ring and cage critical points, respectively. Following the trajectory of gradient path between nuclei, the maximum ρshall be reached and the corresponding coordination is called bond critical point (BCP). At BCP, the total (H_{BCP}), kinetic (G_{BCP}), and potential (V_{BCP}) energy density are functionals of electron density (ρ_{BCP}) with the relationship of $H_{BCP} = G_{BCP}+V_{BCP}$. The magnitude of interatomic interaction is represented by absolute bond degree (BD = H_{BCP}/ρ_{BCP} [47,63]). The distance between nuclei n_1 and n_2 in the form of "n_1-b-n_2" is named as bond length. Through the BDs vs. $|V_{BCP}|/G_{BCP}$ ratios and BLs of M-X (①, ②, and ⑤ in Figure 1a) and X-X (④ and ⑦ in Figure 1a) bonds in bulk, mono-, bi-, and trilayered MX_2, as shown in Figure 4, the exact bonding nature to composition and dimensionality can be determined. The signs of $\nabla^2\rho_{BCP}$ provide details analogous to those found about ρ_{BCP} and have been used to differentiate the closed-shell (CS) and shared-shell (SS) interactions by using the adimensional $|V_{BCP}|/G_{BCP}$ ratio according to the local virial theorem [46] ($h^2/16\pi^2 m\nabla^2\rho_{BCP}=2G_{BCP}+V_{BCP}$, where h and m are the Planck constant and electron mass, respectively). In addition to the pure CS ($|V_{BCP}|/G_{BCP} < 1$) and SS ($|V_{BCP}|/G_{BCP} > 2$) interactions, another region called *transit* CS ($1 < |V_{BCP}|/G_{BCP} < 2$) has been defined [47]. As shown in Figure 4a, the X-X bond

lies in the pure CS region, presenting a local charge-depletion interaction, in other words, forming vdW-like bonding between X atoms. In contrast, the M-X bond lies in the *transit* CS and pure SS regions, presenting the local charge-concentration interactions, namely, forming covalent bonding between M and X atoms.

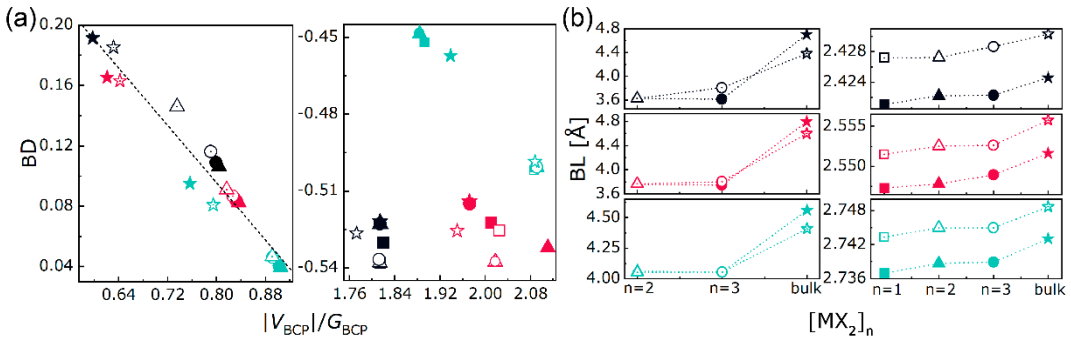

Figure 4. Bond degrees (BD) vs. $|V_{BCP}|/G_{BCP}$ ratios (**a**) and bond lengths (BL) (**b**) of X-X (left panel) and M-X (right panel) bonds in $[MX_2]_n$. Symbols used in plots, solid: MoX_2; hollow: WX_2; black, red, and teal colors: X = S, Se and Te; squares, triangles, circles, and stars: n = 1, 2, 3, and bulk.

The bonding features with the growth of layer thickness can be specified from Figure 4a,b. One can notice that, the vdW bond is sensitive to the layer dimensionality and that, as already evidenced in [63] for other kinds of materials, BDs and |V|/G ratios of X-X bonds are linearly correlated. For a given X, BDs of X-X bonds in bulks (marked as stars) are the highest compared with those in bilayers (marked as triangles) and trilayers (marked as circles). The bulk MoX_2 has higher BD and BL of X-X bond than WX_2, whereas the bi- and trilayered MoX_2 have lower BDs and BLs of X-X bonds than WX_2. This coincides with the bandgap results in Figure 3. Meanwhile, as n goes from two to three, BDs and BLs of X-X bonds in $[MoX_2]_n$ are barely changed, while those in $[WX_2]_n$ decrease and increase respectively, with a declining speed as X goes from S to Te. Additionally, the bulk and layered MoX_2 have smaller absolute BDs and BLs of M-X bonds than WX_2, leading to a stronger W-X bond compared to Mo-X one at any given X, which is consistent with [16]. As n goes from one to three, no significant changes are found for the BDs and BLs of M-X bonds. Thus, except for the Mo-Te bond, the rest M-X bonds in $[MX_2]_n$ are slightly stronger but shorter than those in bulks. As X goes from S to Te, the absolute BDs of X-X and M-X bonds decrease despite the discordances in BLs. Given the linear BD responses of X-X bonds to composition and dimensionality, a dominant position of the interlayer vdW bond in layer-dependent properties is foreseen. Based on Gatti's assumption [64], an atomic expectation value may be equated to a sum of "bond" contributions. In the quest for the structure-properties relationships, we tried to find a relation between the bond degree summation and the dielectric constant. Since in the above discussion structures are fully relaxed and without external perturbation, we have considered the dielectric constant under zero-incident energy $\varepsilon_1(0)$ along the thickening direction. In each unit cell, the numbers of X-X are different, i.e., zero for monolayer, one for bilayer, and two for trilayer. Taking this into account, the weight coefficients l and m have been used to express the absolute BD summation, which is written as $l|BD|_{M\text{-}X}+m|BD|_{X\text{-}X}$. Fitting the $l|BD|_{M\text{-}X}+m|BD|_{X\text{-}X}$ to the $\varepsilon_1(0)$ via equation $y = A + Bx + \cdots + Nx^n + O\left(x^{n+1}\right)$, the maximum coefficient of determination R^2 is achievable by adjusting the l and m at each equation order. As plotted in Figure 5a, the maximum values of R^2 for bulks, bilayers, and trilayers can be located as the equation order goes from first to second and to third. Among them, a cubic equation $y = A + Bx + Cx^2 + Dx^3$ could describe the relationship between bond degree and dielectric constant accurately with the maximum R^2 over 0.99 at l/m = 0.5 and the lowest Akaike and Bayesian information criteria (AIC and BIC) compared with the linear and quadratic equations, as listed in Table 1. This l/m ratio indicates that the X-X bond shares more responsibility in dielectric function than the M-X one, and that share keeps constant no matter the layer thickness. In particular, the R^2 of monolayers are 0.685, 0.974 and

0.999 at the first, second and third orders respectively without adjusting the l/m, since there is only M-X bond, i.e., $m = 0$. At each layer thickness, the absolute BD summation and the $\varepsilon_1(0)$ are inversely related. An advantage in electron excitation is predictable for the entirely weak interatomic interaction, such that explains robust optical response when incident energy is applied. As layer thickness goes up, the fitting curves shift upwards and rightwards, leading to gradually amplified BD summation and $\varepsilon_1(0)$, which evidences the layer-dependent properties of vdW materials. Despite the BD summation of bulk material is in between those of bilayer and trilayer, the $\varepsilon_1(0)$ of the former is the highest, which is consonant with the refraction and absorption results in Figure 3.

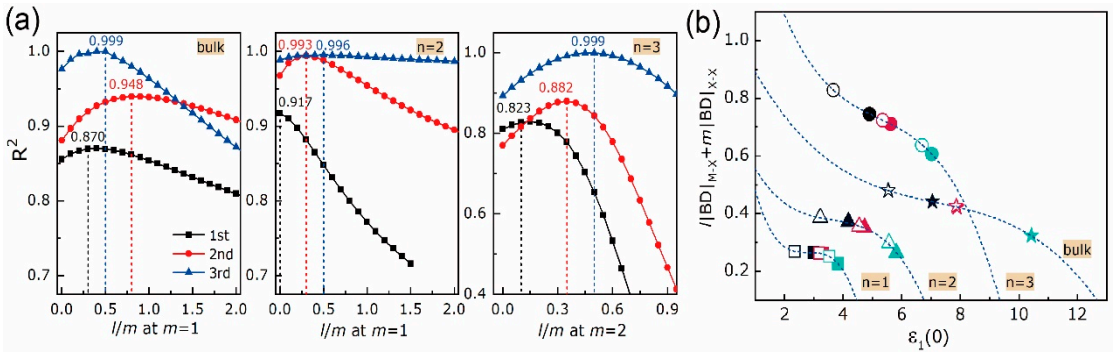

Figure 5. Results of $l|BD|_{M\text{-}X}+m|BD|_{X\text{-}X}$ vs. $\varepsilon_1(0)$ of bulk and $[MX_2]_n$: (**a**) fitting coefficient of determination R^2 vs. l/m ratio as equation order goes from first to second and to third; (**b**) fitting curves of cubic equation $y = A + Bx + Cx^2 + Dx^3$ at maximal R^2. Symbols used in (**b**), solid: MoX_2; hollow: WX_2; black, red and teal colors: X = S, Se and Te; squares, triangles, circles and stars: n = 1, 2, 3, and bulk.

Table 1. Polynomial fitting of $l|BD|_{M\text{-}X}+m|BD|_{X\text{-}X}$ vs. $\varepsilon_1(0)$ via equation $y = A + Bx + \cdots + Nx^n + O\left(x^{n+1}\right)$ of bulk, layered $[MX_2]_n$ and WX_2/MoX_2 heterostructures. Fit quality evaluation criteria, including R^2, AIC and BIC, as well as coefficients A, B, C, D at the first, second and third equation orders.

	Equation Order	R^2	AIC	BIC	A	B	C	D
$[MX_2]_{n=1}$	1st	0.685	−36.76	−37.17	-2.59×10^{-2}	3.39×10^{-1}		
	2nd	0.974	−49.68	−50.3	3.26×10^{-2}	1.78×10^{-1}	-3.32×10^{-2}	
	3rd	0.999	−67.74	−68.58	1.07×10^{0}	-8.54×10^{-1}	3.04×10^{-1}	-3.61×10^{-2}
$[MX_2]_{n=2}$	1st	0.917	−29.4	−29.82	-4.66×10^{-2}	5.56×10^{-1}		
	2nd	0.993	−44.34	−44.96	1.63×10^{-1}	1.32×10^{-1}	-1.96×10^{-1}	
	3rd	0.996	−56.68	−57.51	8.75×10^{-1}	-3.69×10^{-1}	9.45×10^{-2}	-8.46×10^{-3}
$[MX_2]_{n=3}$	1st	0.823	−21.89	−22.31	-5.90×10^{-2}	4.71×10^{-1}		
	2nd	0.882	−22.84	−23.46	7.91×10^{-2}	9.25×10^{-2}	-1.40×10^{-2}	
	3rd	0.999	−60.44	−61.27	1.85×10^{0}	-5.47×10^{-1}	9.55×10^{-2}	-6.10×10^{-3}
Bulk	1st	0.870	−27.53	−27.94	-2.76×10^{-2}	3.81×10^{-1}		
	2nd	0.948	−27.36	−27.98	7.98×10^{-1}	-9.49×10^{-3}	-1.66×10^{-3}	
	3rd	0.999	−54.23	−55.06	1.09×10^{0}	-2.30×10^{-1}	2.89×10^{-2}	-1.34×10^{-3}
WX_2/MoX_2	1st	0.876	−102.3	−100.3	-5.46×10^{-2}	5.63×10^{-1}		
	2nd	0.900	−104.9	−101.9	3.87×10^{-1}	2.40×10^{-2}	-8.45×10^{-3}	
	3rd	0.940	−114.7	−110.7	-5.82×10^{-1}	6.98×10^{-1}	-1.60×10^{-1}	3.03×10^{-3}

4. 2D Heterostructure

4.1. Stability, Electronic, and Optical Properties

The WX_2/MoX_2 (X = S, Se, Te) heterostructures were assembled with the top WX_2 and bottom MoX_2 monolayers taken from their bilayers and denominated from N° 1 to N° 9, as shown in Figure 6a,b. At the interface, X atom from the WX_2 side is directly placed atop M atom from the MoX_2 side, since

this is the most favorable stacking order as explained in [30,51]. After relaxation, the binding energy (E_b) is given by:

$$E_b = 1/2A\left[E_{WX_2/MoX_2} - 1/2\left(E_{WX_2} + E_{MoX_2}\right)\right] \quad (2)$$

where E_{WX_2/MoX_2}, E_{WX_2}, and E_{MoX_2} are the energy of heterostructure and its constitutive top and bottom bilayers, respectively, and A is the interface area. The in-plane lattice mismatch ($\Delta a/a_0$) and E_b of heterostructures are plotted in Figure 6c,d. As can be seen, most of the heterostructures have vdW-like binding energy under both WC-GGA and optB88-vdW functionals, which are in the range of 19–45 meV/Å^2. Two energy values are out of that range, namely the most negative E_b of N°5 ($WSe_2/MoSe_2$) with WC-GGA functional and the least negative E_b of N°9 ($WTe_2/MoTe_2$) with both two functionals. The more negative E_b, the more stable the structure. The N°5 and N°9 are the most stable and unstable respectively despite their smallest lattice mismatches. Additionally, no dependence has been found between structural stability and lattice mismatch since a larger $\Delta a/a_0$ is unnecessarily referring to a smaller E_b and vice versa, such as the N°2 and N°9 cases.

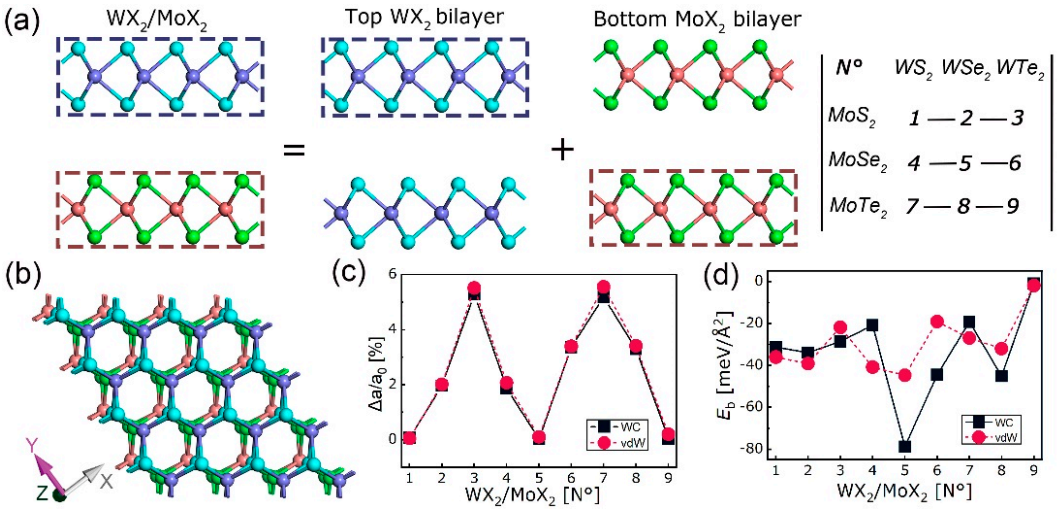

Figure 6. Schemes of WX2/MoX_2 (X = S, Se, Te) heterostructures: (**a**) Side view; (**b**) top view; (**c**) in-plane lattice mismatch $\Delta a/a_0$ in % and (**d**) binding energy E_b in meV/Å^2 at heterointerfaces.

The band structures and density of states (DOS) of the nine heterostructures are shown in Figure 7. The N°1-2 and N°4-6 have direct bandgaps even though their parent bilayers have indirect ones, as shown in Figures S1 and S2. Additionally, the N° 8–9 have indirect bandgaps and the N° 3 and 7 have zero bandgaps. By hetero-stacking, the indirect to direct bandgaps transition becomes possible, as found in [30,52]. The VBMs of N° 1, 5, and 9 are composed of M-d, X-p orbitals of MX_2 (with M being Mo and W), while the CBMs are composed of Mo-d and X-p orbitals of MoX_2. Additionally, the VBMs and CBMs of N° 2, N° 3, and N° 6 are composed of W-d, X-p orbitals of WX_2 and Mo-d, X-p orbitals of MoX_2, respectively. In contrast, the VBMs and CBMs of N° 4 and N° 7 are composed of Mo-d, X-p orbitals of MoX_2 and W-d, and X-p orbitals of WX_2, respectively. A special case is observed for N° 8 whose VBM and CBM are both composed of Mo-d and Te-p orbitals. The MX_2 monolayers contribute exclusively to either CBM or VBM, forming a built-in separation of electrons and holes. This physical detachment favors the collection but recombination of charge carriers.

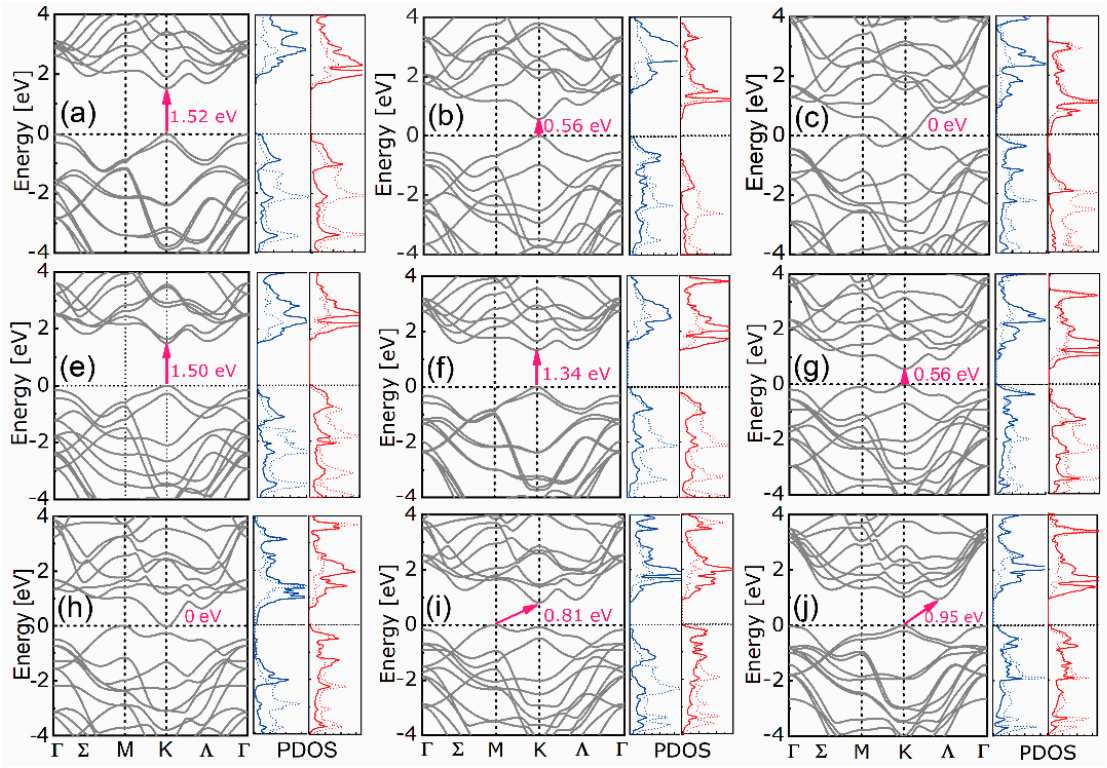

Figure 7. Band structures and density of states (in WX_2, W-d: solid blue; X-p: dash blue; in MoX_2, Mo-d: solid red; X-p: dash red) of N° 1–9 WX_2/MoX_2 (**a**–**j**).

At heterointerfaces, the band alignments, including valence (VBO) and conduction (CBO) band offsets, are obtained by formulae:

$$\Delta E_{VBO}^{WX_2/MoX'_2} = \Delta E_{VBM,C}^{WX_2} - \Delta E_{VBM,C'}^{MoX'_2} + \Delta E_{C,C'} \quad (3)$$

and:

$$\Delta E_{CBO} = \Delta E_g + \Delta E_{VBO} \quad (4)$$

where $\Delta E_{VBM,C}^{WX_2}$ and $\Delta E_{VBM,C'}^{MoX'_2}$ are the energy gaps between core levels, i.e., X/X'-1s, and VBMs of bulk WX_2 and MoX'_2, respectively, and $\Delta E_{C,C'}$ is the binding energy difference between X-1s and X'-1s in WX_2/MoX_2 [61,65]. As plotted in Figure 8b, except for N° 8, the WX_2/MoX_2 belong to type II ("cliff-like") band offsets with opposite signs of VBOs and CBOs. This matches the results in [66] that the common-X hetero-system has type-II band alignment. As a result of that, the VBMs and CBMs are contributed by different sides originating from the metal *d* and chalcogen *p* repulsion. For example, the positive VBOs and negative CBOs of N° 1–3, 5–6, and 9 lead to the WX_2-composed VBMs and MoX_2-composed CBMs. Upon excitation, the excited electrons will jump from WX_2 sides to MoX_2 ones, forming the flow path ❷ in Figure 8a. In contrast, the negative VBOs and positive CBOs of N° 4 and 7 will result in an opposite flow path from MoX_2 sides to WX_2 ones, i.e., path ❶ in Figure 8a. An exception case is found for the N° 8 whose VBM and CBM are both contributed by $MoTe_2$. This type-I ("spike-like") band offset will drive the electrons flow within the $MoTe_2$ monolayer, forming the path ❸ in Figure 8a.

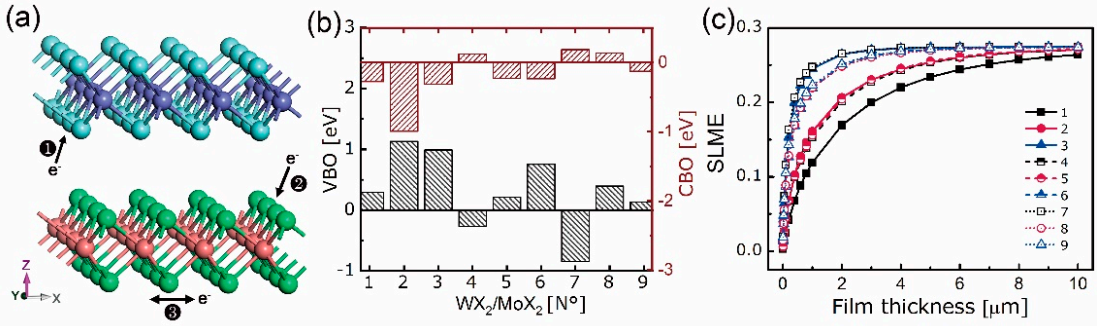

Figure 8. Electron flow path (**a**), valence (black) and conduction (bordeaux) band offsets (**b**) and spectroscopic limited maximum efficiency (**c**) of N° 1–9 WX_2/MoX_2. Path ❶, ❷, and ❸ represent the electron flow from MoX_2 to WX_2, WX_2 to MoX_2, and within $MoTe_2$, respectively.

From the aforementioned observations, the contributions from both the top and bottom monolayers are responsible for its entire performances in electronic and optical fields. As shown in Figure S4 (supplement file), the absorption coefficients of WX_2/MoX_2 are over ~10^5 cm^{-1}. To further characterize the PV ability of WX_2/MoX_2 thin-film, the spectroscopic limited maximum efficiency (SLME) method [67] has been employed. The input power condition is chosen as the AM 1.5G illumination in the wavelength range of 280–1200 nm. Based on the out-of-plane absorption coefficient, the maximum conversion efficiency η_{max} concerning film thickness can be obtained by the output short-circuit current (J_{SC}) and open-circuit voltage (V_{OC}). The fast increasing J_{SC} and slow decreasing V_{OC}, originating from charge carrier enrichment and recombination, respectively, give rise to a continuously growing η_{max} with the film thickness. As shown in Figure 8c, the η_{max} of WX_2/MoX_2 all converge to certain values which are over 25%, and accordingly, that with small atomic number is lower than that with large atomic number.

4.2. Electron Density Analysis

The distributions of electron density and its Laplacian of WS_2/MoS_2 are shown in Figure S5 (Supplement file), which is used as an example. The in-plane lattice mismatch (*lm*) in heterostructures and the corresponding signs in the constitutive bilayers are listed in Table 2, where the "+" sign means tensile strain and the "-" sign means compressive strain. The BDs with respect to $|V_{BCP}|/G_{BCP}$ ratios and BLs of X-X and M-X bonds in heterostructures and the constitutive top and bottom bilayers are plotted in Figures 9 and 10, respectively. Based on the $|V_{BCP}|/G_{BCP}$ ratio, X-X bonds have vdW bonding and M-X bonds have covalent bonding, which is the same as those in primitive layered and bulk structures. Upon the construction of heterostructures, the linear correlation between BDs and $|V_{BCP}|/G_{BCP}$ ratios of X-X bonds is maintained, underlying a linear responsivity of vdW bonding force to *lm*. Irrespective of the X-X bond, its BL (Figure 9d) and E_b (Figure 6d) are correlated; smaller BL corresponds to less negative E_b. For example, the $WTe_2/MoTe_2$, with the shortest Te-Te bond at the interface, has the least negative E_b despite its small *lm* since stability is irrelevant to *lm*, as discussed before.

Table 2. In-plane lattice mismatch (*lm*) in % in WX_2/MoX_2 and the signs in the constitutive top WX_2 (′) and bottom MoX_2 (″) bilayers. The "-" and "+" represent compressive and tensile strain, respectively.

WX_2/MoX_2	**N°**	**1**	**2**	**3**	**4**	**5**	**6**	**7**	**8**	**9**
	lm	**0.06**	**1.96**	**5.30**	**1.88**	**0.02**	**3.36**	**5.19**	**3.30**	**0.04**
Top $[WX_2]_{n=2}$	X	S	Se	Te	S	Se	Te	S	Se	Te
	N°	1′	2′	3′	4′	5′	6′	7′	8′	9′
	Sign	-	-	-	+	-	-	+	+	-
Bottom $[MoX_2]_{n=2}$	X	S	S	S	Se	Se	Se	Te	Te	Te
	N°	1″	2″	3″	4″	5″	6″	7″	8″	9″
	sign	+	+	+	-	+	+	-	-	+

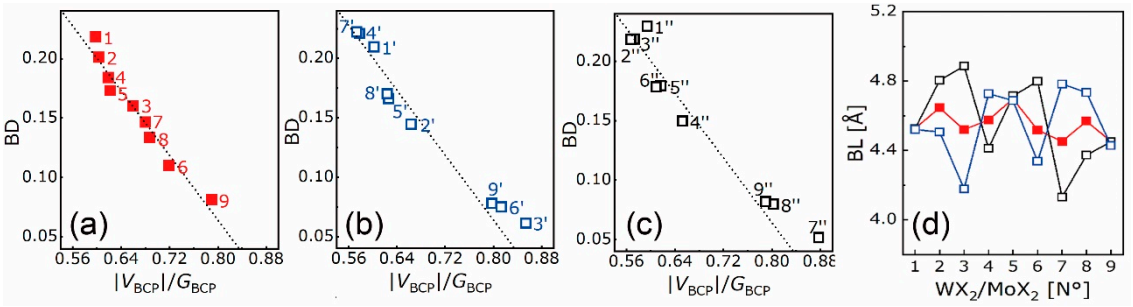

Figure 9. BDs vs. $|V_{BCP}|/G_{BCP}$ ratios of X-X bonds in N° 1–9 WX_2/MoX_2 (red) (**a**), top WX_2 bilayers (blue) (**b**), bottom MoX_2 bilayers (black) (**c**), and their BLs (**d**).

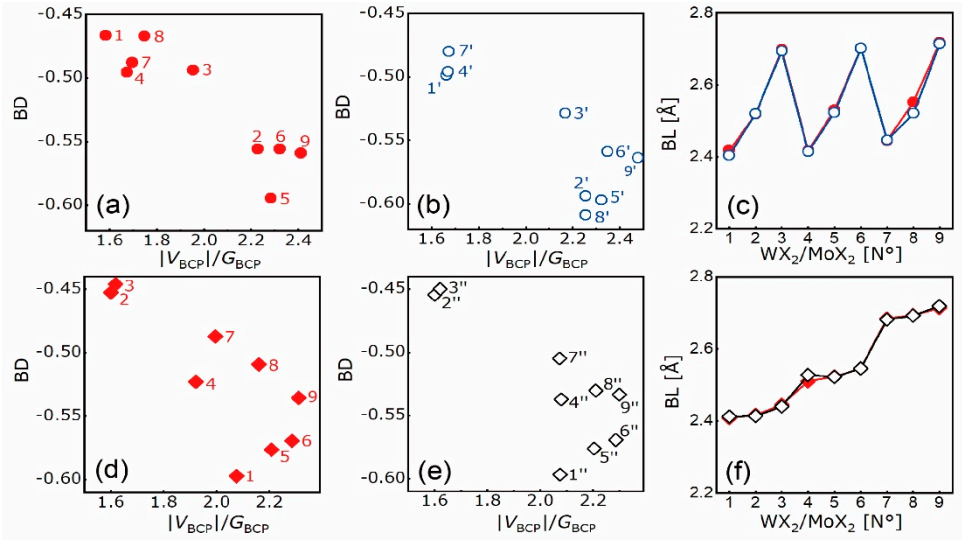

Figure 10. BDs vs. $|V_{BCP}|/G_{BCP}$ ratios of W-X bonds in N°1-9 WX_2/MoX_2 (red) (**a**), top WX_2 bilayers (blue) (**b**) and their BLs (**c**). BDs vs. $|V_{BCP}|/G_{BCP}$ ratios of Mo-X bonds in WX_2/MoX_2 (red) (**d**), bottom MoX_2 bilayers (black) (**e**), and their BLs (**f**).

By comparing the bonding nature in heterostructure and its constitutive bilayers, the influence of hetero-stacking on opposite sublayers can be drawn. Hereafter, bonds in the constitutive top and bottom bilayers are marked by signs (′) and (″), respectively. In top WX_2 bilayers, the BDs and BLs of S-S (N° 1′, 4′, 7′), Se-Se (N° 2′, 5′, 8′), Te-Te (N° 3′, 6′, 9′) and W-S (N°1′, 4′, 7′) bonds increase as the *lm* goes from "-" to "+". This holds for S-S (N° 2″, 3″), Se-Se (N° 4″, 5″, 6″), Te-Te (N° 7″, 8″, 9″) and Mo-S (N° 1″, 2″, 3″) bonds in bottom MoX_2 bilayers as well. In contrast, the BDs and BLs of W-Se (N°2′, 5′, 8′), W-Te (N° 3′, 6′, 9′), Mo-Se (N° 4″, 6″), and Mo-Te (N° 7″, 8″, 9″) bonds decrease and increase, respectively, as the *lm* goes from "-" to "+". Two exceptional cases are found for the N° 1″ S-S and N° 5″ Mo-Se bonds, which corresponds to the abruptly intensified N° 1″ Mo-S and weakened N° 5″ Se-Se. The BDs and BLs are positively correlated for X-X and M-S bonds, while negatively correlated for M-Se and M-Te bonds. Compared with X-X bonds, W-X and Mo-X ones have less evident BL changes. When $lm < 0$ and $lm > 0$, the absolute BDs of X-X and M-X bonds go the opposite way, such as N° 3′, 6′, 9′ bonds at WTe_2 bilayers and N° 1″, 2″, 3″ bonds at MoS_2 bilayers. Consequently, under tensile strain, X-X and M-S bonds tend to weaken and elongate while M-Se/Te ones tend to strengthen and elongate; under compressive strain, X-X and M-S bonds tend to strengthen and shorten while M-Se/Te ones tend to weaken and shorten. Additionally, as chalcogen atomic number goes up, BDs of M-X bonds first decrease and then increase with continuously increasing BLs, whereas BDs and BLs of X-X bonds decrease continuously. Additionally, the BD is more susceptible to compressive strain than tensile strain, as a result of the expanding BD difference under the former (e.g., N° 7″ and 8″ of $MoTe_2$) while the shrinking one under the latter (e.g., N° 2″ and 3″ of MoS_2). The discordant BD

evolution to strains explains the separate generation of electrons and holes in the opposite monolayers, which will be discussed below.

Given the strain-induced bonding behaviors of the top and bottom bilayers, as illustrated above, the electronic performances of heterostructures can be identified. The N° 1′-3′, 5′-6′, and 9′ X-X bonds in WX_2 bilayers (Figure 9b) have smaller BDs than the N° 1′′-3′′, 5′′-6′′, and 9′′ ones in MoX_2 bilayers (Figure 9c), leading to a stronger capability of electron excitation in WX_2 monolayers than MoX_2 ones after stacking them together. In the meantime, the absolute BDs of W-X bonds in WX_2/MoX_2 (Figure 10a) are lower than those in WX_2 bilayers (Figure 10b), whereas those of Mo-X bonds in WX_2/MoX_2 (Figure 10d) overlap with those in MoX_2 bilayers (Figure 10e). Therefore, after stacking two monolayers together, the interatomic interaction of W-X bond is undermined while that of Mo-X bond is unchanged. Coupling with the prevalent excitation in X-X bond, a superior electron excitation shall be located in the WX_2 monolayer, followed by the electron transition to the MoX_2 monolayer through M-d and X-p orbitals. This is the underlying mechanism for path ❷ mentioned above. Similarly, the smaller BDs of N° 4′′ and 7′′ X-X bonds than those of N° 4′ and 7′ ones would end up with a superior capability in electron excitation at MoX_2 parts. Additionally, the absolute BDs of Mo-X bonds decrease while those of W-X bonds are barely changed after stacking. For the same reason, abundant electrons could be located at the MoX_2 monolayer and flow to the WX_2 monolayer. Nevertheless, the smaller BD of N° 8′′ X-X bond than that of N° 8′ one brings the preference of electron excitation to the MoX_2 monolayer. Though the BD of W-X bond increases further than that of Mo-X one after stacking, the preeminent position of X-X bond in electron excitation will drive the electron flowing within the MoX_2 monolayer. Thus, path ❶ and ❸ are explained.

From Figure 9d, the BLs of X-X bonds in heterostructures are close to the average values of those in the constitutive bilayers, and within the range of 4.45–4.70 Å. Additionally, no consistency is found between BDs and BLs of X-X bonds as the *lm* varies. For instance, in the N° 1–3 cases where MoS_2 is fixed as the bottom monolayer, the BDs of X-X bonds decline linearly while the BLs first increase and then decrease with the *lm*. To further elucidate the relationship between bond geometry and binding energy at interfaces, the bond angles (BA) $\angle n_1 b n_2$ of X-X and M-X bonds in the form of "n_1-b-n_2" are discussed, as plotted in Figure 11. As can be seen, the BAs of X-X bonds in the constitutive bilayers are close to 180° and overlap with each other, whereas those in heterostructures are lower than 180° and interestingly, are inversely correlated to the *lm*. On the contrary, the BAs of W-X and Mo-X bonds have barely visible differences between those in heterostructures and two relevant bilayers. The X-X bond is keen on lattice mismatch by the BCP migration towards the atomic end with high electronegativity. In other words, the "b" in the form above shifts to either n_1 or n_2. The X-X bond encounters lattice strain by BA adjustment, such that the interlayer distance is maintained within a certain range. Thereupon, the mechanisms for vdW heterostructure free of lattice constraint are concretized by the positively correlated bond length and binding energy, and the negatively-correlated bond angle and lattice mismatch.

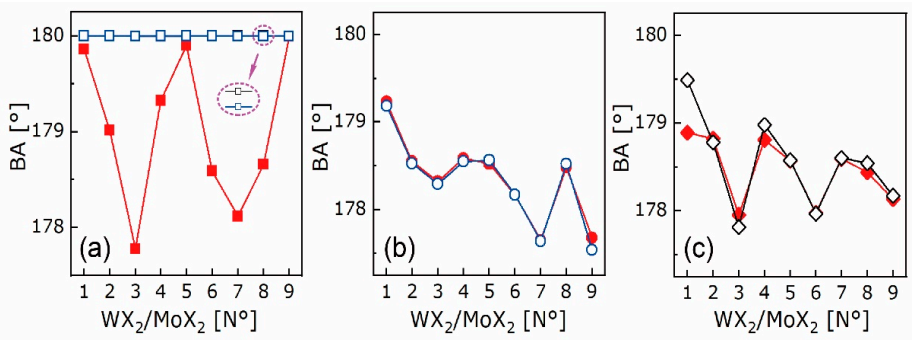

Figure 11. Bond angles (BA) of X-X (**a**), W-X (**b**), Mo-X (**c**) bonds in N° 1–9 WX_2/MoX_2 (red), top WX_2 bilayers (blue), and bottom MoX_2 bilayers (black).

To examine the applicability of the above cubic relationship between absolute BD summation $l|BD|_{M\text{-}X}+m|BD|_{X\text{-}X}$ and static dielectric constant $\varepsilon_1(0)$ in WX_2/MoX_2 heterostructures and the constitutive bilayers with interfacial strains, the polynomial equations with different orders are also used by changing the l/m ratio, as plotted in Figure 12a. It needs mentioning that in WX_2/MoX_2, the contribution of M-X bonds to the BD summation is set to the average value of Mo-X and W-X bond, namely, $l|BD|_{M\text{-}X} = l/2(|BD|_{Mo\text{-}X}+|BD|_{W\text{-}X})$. As equation order goes from first to third, the R^2 increases accompanied by an enlarging l/m ratio. At the corresponding maximum value, the AIC and BIC of the third equation order are the lowest compared with those of other orders, as listed in Table 1. The fitting curve and coefficients are shown in Figure 12b and Table 1, respectively, on behalf of the well-described cubic relationship ($R^2 = 0.960$). Compared with the l/m of primitive bulk and layered MX_2 ($l/m = 0.5$), that of structures subjected to strain ($l/m = 0.3$) is smaller, as well as the R^2, which could be explained by the strain-induced deformation in interatomic interactions of X-X bonds as well as the uneven interactions between W-X and Mo-X bonds. Once strain exists, a superior capability of X-X bond in responding to the electromagnetic field is foreseen by sharing more responsibility for dielectric function than M-X bond. Its prompt response is coherent with the linear reaction to strain and hetero-stacking, as shown in Figure 9a. The decrease of interatomic interaction goes along with the increase of dielectric constant. This is the reason for heterostructure with a higher chalcogen atomic number having better optical behavior, as the SLME in Figure 8c illustrates. Indeed, quantifying the relationship between optical and bonding properties is of great meaning for interpreting theunderlying bonding mechanism and predicting the macroscopic development of vdW material whose lattice and strain changes. Accordingly, the resulting correlation of structural engineering to interatomic interaction allows us to anticipate the potentiality to achieve equivalent optical response but with fewer material expenses.

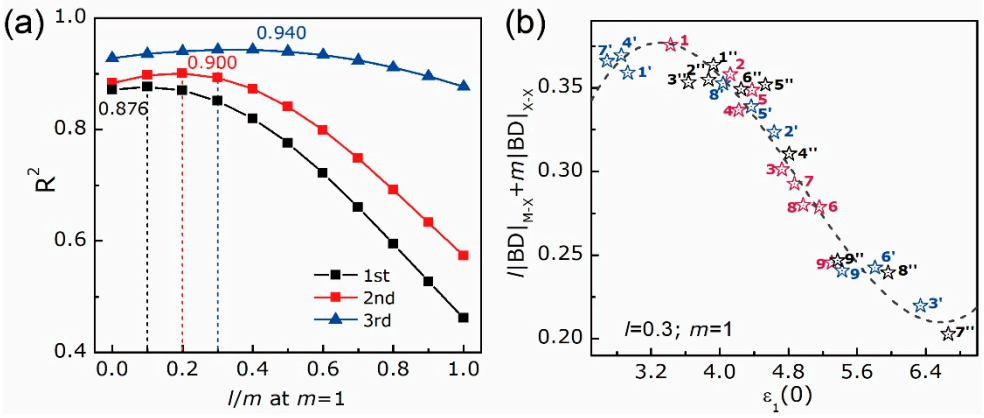

Figure 12. Results of $l|BD|_{M\text{-}X}+m|BD|_{X\text{-}X}$ vs. $\varepsilon_1(0)$ of WX_2/MoX_2 and the constitutive bilayers: (**a**) fitting coefficient of determination R^2 vs. l/m ratio as equation order goes from first to second and to third; (**b**) cubic fitting curves at maximum R^2 (=0.940) with red, blue, and black colors representing heterostructures, top WX_2 (') and bottom MoX_2 (") bilayers, respectively.

5. Conclusions

DFT calculations of MX_2 homo- and heterostructures, the layer-dependent structural, electronic and optical properties have been performed. In layered MX_2, a broadening bandgap and its indirect-direct transition happen with the thinning of thickness. The widespread bandgaps as X goes from S to Te envisages designs of lightweight and diverse PV cells. Based on the QTAIM, electron density analyses are detailed to connect microscopic interaction with macroscopic electromagnetic behaviors. The relationship between optical and bonding properties can be formulated by a cubic equation relating to weighted BD summation and static dielectric constant. Irrespective of structure and strain, X-X bonds lie in charge-depletion region with linearly correlated BDs and $|V|/G$ ratios, whereas M-X bonds lie in charge-accumulation region with barely changed BDs as layer thickness varies. In effect,

the layer-dependent electronic and optical properties are mainly attributed to the X-X bond due to its prompt responsivity to strain and hetero-stacking. The WX_2/MoX_2 have type-II band offsets with the maximum conversion efficiency of over 25% owing to the exclusive distribution of electrons and holes in separate sublayers. Positively correlated vdW bond length and binding force, and negatively-correlated vdW bond angle and lattice mismatch are the reasons for vdW structures free of lattice constraint, maintaining interlayer distances within ranges. Our findings contribute to increasing the knowledge of the TMDs materials and offering a new approach for the development of the 2D stacked thin-film solar cells.

Supplementary Materials: The following are available online at https://doi.org/10.5281/zenodo.4158700, Table S1: Calculated lattice constants *a* and *c* and indirect bandgaps E_g of bulk MX_2 (X = S, Se, Te) by using WC-GGA, optB88-vdW and mBJ functionals, as well as other theoretical "(c)" and experimental "(e)" data. Figure S1: Band structures of bulk, mono-, bi- and tri-layered MoS_2 (a), $MoSe_2$ (b), and $MoTe_2$ (c) calculated by WC-GGA functional. Figure S2: Band structures of bulk, mono-, bi-, and tri-layered WS_2 (a), WSe_2 (b), and WTe_2 (c) calculated by the WC-GGA functional. Figure S3: Electron density (a) and Laplacian (b) distributions of bulk, mono-, bi, and tri-layered MoS_2. Labels "b", "r", and "c" represent the bond, ring, and cage critical points at the zero-flux surface, respectively. Figure S4: In-plane (*xx*) and out-of-plane (zz) refractive indices *n* (a), absorption coefficients α (b), and loss tangents (c) of N° 1–9 heterostructures. Figure S5: Electron density (a) and Laplacian (b) distributions of the N° 1 WS_2/MoS_2 heterostructure along the <110> plane (a)–(i). Labels "b", "r", and "c" represent the bond, ring, and cage critical points at the zero-flux surface, respectively.

Author Contributions: Conceptualization: M.-C.R., P.B., and P.J.; methodology: P.J.; software: P.J.; formal analysis and original draft preparation: P.J.; review and editing: M.-C.R., P.B.; supervision: M.-C.R. and P.B. All authors have read and agreed to the published version of the manuscript.

Funding: This research is financially supported by the China Scholarship Council (CSC).

Acknowledgments: This work was granted access to the HPC resources of the Centre Informatique National de l'Enseignement Supérieur (CINES), Montpellier, France under allocation A0050806881 made by the Grand Equipement National de Calcul Intensif (GENCI). It was also granted access to the HPC resources of Aix-Marseille Université financed by the project Equip@Meso (ANR-10-EQPX-29-01) of the program "Investissements d'Avenir" supervised by the Agence Nationale de la Recherche.

Conflicts of Interest: The authors declare no conflict of interest.

References

1. Novoselov, K.S. Electric Field Effect in Atomically Thin Carbon Films. *Science* **2004**, *306*, 666–669. [CrossRef] [PubMed]
2. Jariwala, D.; Davoyan, A.R.; Wong, J.; Atwater, H.A. Van der Waals Materials for Atomically-Thin Photovoltaics: Promise and Outlook. *ACS Photonics* **2017**, *4*, 2962–2970. [CrossRef]
3. Brahma, M.; Kabiraj, A.; Saha, D.; Mahapatra, S. Scalability assessment of Group-IV mono-chalcogenide based tunnel FET. *Sci. Rep.* **2018**, *8*, 5993. [CrossRef] [PubMed]
4. Chhowalla, M.; Shin, H.S.; Eda, G.; Li, L.-J.; Loh, K.P.; Zhang, H. The chemistry of two-dimensional layered transition metal dichalcogenide nanosheets. *Nat. Chem.* **2013**, *5*, 263–275. [CrossRef] [PubMed]
5. Lukowski, M.A.; Daniel, A.S.; Meng, F.; Forticaux, A.; Li, L.; Jin, S. Enhanced Hydrogen Evolution Catalysis from Chemically Exfoliated Metallic MoS_2 Nanosheets. *J. Am. Chem. Soc.* **2013**, *135*, 10274–10277. [CrossRef] [PubMed]
6. Long, M.; Wang, P.; Fang, H.; Hu, W. Progress, Challenges, and Opportunities for 2D Material Based Photodetectors. *Adv. Funct. Mater.* **2019**, *29*, 1803807. [CrossRef]
7. Xu, M.; Liang, T.; Shi, M.; Chen, H. Graphene-Like Two-Dimensional Materials. *Chem. Rev.* **2013**, *113*, 3766–3798. [CrossRef]
8. Wu, F.; Li, Q.; Wang, P.; Xia, H.; Wang, Z.; Wang, Y.; Luo, M.; Chen, L.; Chen, F.; Miao, J.; et al. High efficiency and fast van der Waals hetero-photodiodes with a unilateral depletion region. *Nat. Commun.* **2019**, *10*, 4663. [CrossRef]
9. Tan, C.; Lai, Z.; Zhang, H. Ultrathin two-dimensional multinary layered metal chalcogenide nanomaterials. *Adv. Mater.* **2017**, *29*, 1701392. [CrossRef]
10. Jariwala, D.; Marks, T.J.; Hersam, M.C. Mixed-dimensional van der Waals heterostructures. *Nat. Mater.* **2017**, *16*, 170–181. [CrossRef] [PubMed]

11. Jiang, H. Electronic band structures of Molybdenum and Tungsten dichalcogenides by the *GW* approach. *J. Phys. Chem. C* **2012**, *116*, 7664–7671. [CrossRef]
12. Wang, S.; Tian, H.; Ren, C.; Yu, J.; Sun, M. Electronic and optical properties of heterostructures based on transition metal dichalcogenides and graphene-like zinc oxide. *Sci. Rep.* **2018**, *8*, 12009. [CrossRef] [PubMed]
13. Py, M.A.; Haering, R.R. Structural destabilization induced by lithium intercalation in MoS $_2$ and related compounds. *Can. J. Phys.* **1983**, *61*, 76–84. [CrossRef]
14. Huang, H.H.; Fan, X.; Singh, D.J.; Chen, H.; Jiang, Q.; Zheng, W.T. Controlling phase transition for single-layer MTe_2 (M = Mo and W): modulation of the potential barrier under strain. *Phys. Chem. Chem. Phys.* **2016**, *18*, 4086–4094. [CrossRef]
15. Li, J.; Medhekar, N.V.; Shenoy, V.B. Bonding Charge Density and Ultimate Strength of Monolayer Transition Metal Dichalcogenides. *J. Phys. Chem. C* **2013**, *117*, 15842–15848. [CrossRef]
16. Huang, L.-F.; Zeng, Z. Roles of Mass, Structure, and Bond Strength in the Phonon Properties and Lattice Anharmonicity of Single-Layer Mo and W Dichalcogenides. *J. Phys. Chem. C* **2015**, *119*, 18779–18789. [CrossRef]
17. Voiry, D.; Mohite, A.; Chhowalla, M. Phase engineering of transition metal dichalcogenides. *Chem. Soc. Rev.* **2015**, *44*, 2702–2712. [CrossRef]
18. Wilson, J.A.; Yoffe, A.D. The transition metal dichalcogenides discussion and interpretation of the observed optical, electrical and structural properties. *Adv. Phys.* **1969**, *18*, 193–335. [CrossRef]
19. Heising, J.; Kanatzidis, M.G. Exfoliated and Restacked MoS_2 and WS_2: Ionic or Neutral Species? Encapsulation and Ordering of Hard Electropositive Cations. *J. Am. Chem. Soc.* **1999**, *121*, 11720–11732. [CrossRef]
20. Eda, G.; Fujita, T.; Yamaguchi, H.; Voiry, D.; Chen, M.; Chhowalla, M. Coherent Atomic and Electronic Heterostructures of Single-Layer MoS_2. *ACS Nano* **2012**, *6*, 7311–7317. [CrossRef]
21. Cheng, X.; Li, Y.; Shang, J.; Hu, C.; Ren, Y.; Liu, M.; Qi, Z. Thickness-dependent phase transition and optical behavior of MoS2 films under high pressure. *Nano Res.* **2018**, *11*, 855–863. [CrossRef]
22. Kumar, A.; Ahluwalia, P.K. Electronic structure of transition metal dichalcogenides monolayers 1H-MX2 (M = Mo, W; X = S, Se, Te) from ab-initio theory: new direct band gap semiconductors. *Eur. Phys. J. B* **2012**, *85*, 186. [CrossRef]
23. Mak, K.F.; Lee, C.; Hone, J.; Shan, J.; Heinz, T.F. Atomically Thin MoS 2: A New Direct-Gap Semiconductor. *Phys. Rev. Lett.* **2010**, *105*, 136805. [CrossRef]
24. Splendiani, A.; Sun, L.; Zhang, Y.; Li, T.; Kim, J.; Chim, C.-Y.; Galli, G.; Wang, F. Emerging Photoluminescence in Monolayer MoS $_2$. *Nano Lett.* **2010**, *10*, 1271–1275. [CrossRef]
25. Ruppert, C.; Aslan, O.B.; Heinz, T.F. Optical properties and band gap of single- and few-layer $MoTe_2$ crystals. *Nano Lett.* **2014**, *14*, 6231–6236. [CrossRef]
26. Latzke, D.W.; Zhang, W.; Suslu, A.; Chang, T.-R.; Lin, H.; Jeng, H.-T.; Tongay, S.; Wu, J.; Bansil, A.; Lanzara, A. Electronic structure, spin-orbit coupling, and interlayer interaction in bulk MoS 2 and WS 2. *Phys. Rev. B* **2015**, *91*, 235202. [CrossRef]
27. Gong, Y.; Lin, J.; Wang, X.; Shi, G.; Lei, S.; Lin, Z.; Zou, X.; Ye, G.; Vajtai, R.; Yakobson, B.I.; et al. Vertical and in-plane heterostructures from WS2/MoS2 monolayers. *Nat. Mater.* **2014**, *13*, 1135–1142. [CrossRef]
28. Huang, C.; Wu, S.; Sanchez, A.M.; Peters, J.J.P.; Beanland, R.; Ross, J.S.; Rivera, P.; Yao, W.; Cobden, D.H.; Xu, X. Lateral heterojunctions within monolayer MoSe2–WSe2 semiconductors. *Nat. Mater.* **2014**, *13*, 1096–1101. [CrossRef]
29. Lee, C.-H.; Lee, G.-H.; van der Zande, A.M.; Chen, W.; Li, Y.; Han, M.; Cui, X.; Arefe, G.; Nuckolls, C.; Heinz, T.F.; et al. Atomically thin p–n junctions with van der Waals heterointerfaces. *Nat. Nanotechnol.* **2014**, *9*, 676–681. [CrossRef]
30. Amin, B.; Singh, N.; Schwingenschlögl, U. Heterostructures of transition metal dichalcogenides. *Phys. Rev. B* **2015**, *92*, 075439. [CrossRef]
31. Kahn, E.; Liu, M.; Zhang, T.; Liu, H.; Fujisawa, K.; Bepete, G.; Ajayan, P.M.; Terrones, M. Functional hetero-interfaces in atomically thin materials. *Mater. Today* **2020**, *37*, 74–92. [CrossRef]
32. Gupta, A.; Sakthivel, T.; Seal, S. Recent development in 2D materials beyond graphene. *Prog. Mater. Sci.* **2015**, *73*, 44–126. [CrossRef]
33. Wang, X.; Sun, Y.; Liu, K. Chemical and structural stability of 2D layered materials. *2D Mater.* **2019**, *6*, 042001. [CrossRef]

34. Li, J.; Huang, L.; Hou, J.; Wu, X.; Niu, J.; Chen, G.; Gong, J.; Kong, Y.; Xiao, X. Effects of substrate orientation and solution movement in chemical bath deposition on Zn(O,S) buffer layer and Cu(In,Ga)Se2 thin film solar cells. *Nano Energy* **2019**, *58*, 427–436. [CrossRef]
35. Luo, Z.; Ouyang, Y.; Zhang, H.; Xiao, M.; Ge, J.; Jiang, Z.; Wang, J.; Tang, D.; Cao, X.; Liu, C.; et al. Chemically activating MoS2 via spontaneous atomic palladium interfacial doping towards efficient hydrogen evolution. *Nat. Commun.* **2018**, *9*, 2120. [CrossRef] [PubMed]
36. Zhang, X.; Zhou, F.; Zhang, S.; Liang, Y.; Wang, R. Engineering MoS $_2$ Basal Planes for Hydrogen Evolution via Synergistic Ruthenium Doping and Nanocarbon Hybridization. *Adv. Sci.* **2019**, *6*, 1900090. [CrossRef] [PubMed]
37. Cao, D.; Ye, K.; Moses, O.A.; Xu, W.; Liu, D.; Song, P.; Wu, C.; Wang, C.; Ding, S.; Chen, S.; et al. Engineering the In-Plane Structure of Metallic Phase Molybdenum Disulfide *via* Co and O Dopants toward Efficient Alkaline Hydrogen Evolution. *ACS Nano* **2019**, *13*, 11733–11740. [CrossRef] [PubMed]
38. Su, L.; Yu, Y.; Cao, L.; Zhang, Y. Effects of substrate type and material-substrate bonding on high-temperature behavior of monolayer WS2. *Nano Res.* **2015**, *8*, 2686–2697. [CrossRef]
39. Ghorbani-Asl, M.; Zibouche, N.; Wahiduzzaman, M.; Oliveira, A.F.; Kuc, A.; Heine, T. Electromechanics in MoS_2 and WS_2: nanotubes vs. monolayers. *Sci. Rep.* **2013**, *3*, 2961. [CrossRef]
40. Kou, L.; Frauenheim, T.; Chen, C. Nanoscale Multilayer Transition-Metal Dichalcogenide Heterostructures: Band Gap Modulation by Interfacial Strain and Spontaneous Polarization. *J. Phys. Chem. Lett.* **2013**, *4*, 1730–1736. [CrossRef]
41. Zhao, Y.-H.; Yang, F.; Wang, J.; Guo, H.; Ji, W. Continuously tunable electronic structure of transition metal dichalcogenides superlattices. *Sci. Rep.* **2015**, *5*, 8356. [CrossRef]
42. Klimeš, J.; Bowler, D.R.; Michaelides, A. Chemical accuracy for the van der Waals density functional. *J. Phys. Condens. Matter* **2009**, *22*, 022201. [CrossRef]
43. Tao, J.; Perdew, J.P.; Tang, H.; Shahi, C. Origin of the size-dependence of the equilibrium van der Waals binding between nanostructures. *J. Chem. Phys.* **2018**, *148*, 074110. [CrossRef] [PubMed]
44. Zhang, G.-X.; Tkatchenko, A.; Paier, J.; Appel, H.; Scheffler, M. van der Waals interactions in ionic and semiconductor solids. *Phys. Rev. Lett.* **2011**, *107*, 245501. [CrossRef]
45. Ci, P.; Chen, Y.; Kang, J.; Suzuki, R.; Choe, H.S.; Suh, J.; Ko, C.; Park, T.; Shen, K.; Iwasa, Y.; et al. Quantifying van der Waals Interactions in Layered Transition Metal Dichalcogenides from Pressure-Enhanced Valence Band Splitting. *Nano Lett.* **2017**, *17*, 4982–4988. [CrossRef]
46. Bader, R.F.W. A quantum theory of molecular structure and its applications. *Chem. Rev.* **1991**, *91*, 893–928. [CrossRef]
47. Espinosa, E.; Alkorta, I.; Elguero, J.; Molins, E. From weak to strong interactions: A comprehensive analysis of the topological and energetic properties of the electron density distribution involving X–H F–Y systems. *J. Chem. Phys.* **2002**, *117*, 5529–5542. [CrossRef]
48. Mitroy, J.; Safronova, M.S.; Clark, C.W. Theory and applications of atomic and ionic polarizabilities. *J. Phys. B At. Mol. Opt. Phys.* **2010**, *43*, 202001. [CrossRef]
49. Atkins, P.W.; De Paula, J. *Atkins' Physical Chemistry*, 9th ed.; Oxford University Press: Oxford, UK; New York, NY, USA, 2010; ISBN 978-0-19-954337-3.
50. Morita, K.; Davies, D.W.; Butler, K.T.; Walsh, A. Modeling the dielectric constants of crystals using machine learning. *J. Chem. Phys.* **2020**, *153*, 024503. [CrossRef]
51. Hu, X.; Kou, L.; Sun, L. Stacking orders induced direct band gap in bilayer $MoSe_2$-WSe_2 lateral heterostructures. *Sci. Rep.* **2016**, *6*, 31122. [CrossRef]
52. Terrones, H.; López-Urías, F.; Terrones, M. Novel hetero-layered materials with tunable direct band gaps by sandwiching different metal disulfides and diselenides. *Sci. Rep.* **2013**, *3*, 1549. [CrossRef]
53. Wang, F.; Wang, J.; Guo, S.; Zhang, J.; Hu, Z.; Chu, J. Tuning coupling behavior of stacked heterostructures based on MoS2, WS2, and WSe2. *Sci. Rep.* **2017**, *7*, 44712. [CrossRef]
54. Blaha, P.; Schwarz, K.; Madsen, G.K.H.; Kvasnicka, D.; Luitz, J. *WIEN2k: An Augmented Plane Wave Local Orbitals Program for Calculating Crystal Properties*; Karlheinz Schwarz; Technische Universität Wien: Vienna, Austria, 2001; ISBN 3-9501031-1-2.
55. Wu, Z.; Cohen, R.E. More accurate generalized gradient approximation for solids. *Phys. Rev. B* **2006**, *73*, 235116. [CrossRef]

56. Tran, F.; Blaha, P. Accurate band gaps of semiconductors and insulators with a semilocal exchange-correlation potential. *Phys. Rev. Lett.* **2009**, *102*, 226401. [CrossRef]
57. Monkhorst, H.J.; Pack, J.D. Special points for Brillouin-zone integrations. *Phys. Rev. B* **1976**, *13*, 5188–5192. [CrossRef]
58. Zeng, F.; Zhang, W.-B.; Tang, B.-Y. Electronic structures and elastic properties of monolayer and bilayer transition metal dichalcogenides MX_2 (M = Mo, W; X = O, S, Se, Te): A comparative first-principles study. *Chin. Phys. B* **2015**, *24*, 097103. [CrossRef]
59. Otero-de-la-Roza, A.; Johnson, E.R.; Luaña, V. Critic2: A program for real-space analysis of quantum chemical interactions in solids. *Comput. Phys. Commun.* **2014**, *185*, 1007–1018. [CrossRef]
60. Jiang, P.; Boulet, P.; Record, M.-C. A DFT study of the electronic, optical and topological properties of free and biaxially strained $CuIn_{1-x}Al_xSe_2$. *J. Mater. Chem. C* **2019**, *7*, 5803–5815. [CrossRef]
61. Jiang, P.; Record, M.-C.; Boulet, P. First-principles calculations on $CuInSe_2$/AlP heterostructures. *J. Mater. Chem. C* **2020**, *8*, 4732–4742. [CrossRef]
62. Gusakova, J.; Wang, X.; Shiau, L.L.; Krivosheeva, A.; Shaposhnikov, V.; Borisenko, V.; Gusakov, V.; Tay, B.K. Electronic Properties of Bulk and Monolayer TMDs: Theoretical Study Within DFT Framework (GVJ-2e Method). *Phys. Status Solidi A* **2017**, *214*, 1700218. [CrossRef]
63. Yang, H.; Boulet, P.; Record, M.-C. A rapid method for analyzing the chemical bond from energy densities calculations at the bond critical point. *Comput. Theor. Chem.* **2020**, *1178*, 112784. [CrossRef]
64. Gatti, C. Chemical bonding in crystals: new directions. *Z. Für Krist. - Cryst. Mater.* **2005**, *220*. [CrossRef]
65. Kowalczyk, S.P.; Cheung, J.T.; Kraut, E.A.; Grant, R.W. CdTe-HgTe (-1-1-1) heterojunction valence-band discontinuity: A common-anion-rule contradiction. *Phys. Rev. Lett.* **1986**, *56*, 1605–1608. [CrossRef]
66. Kang, J.; Tongay, S.; Zhou, J.; Li, J.; Wu, J. Band offsets and heterostructures of two-dimensional semiconductors. *Appl. Phys. Lett.* **2013**, *102*, 012111. [CrossRef]
67. Yu, L.; Zunger, A. Identification of potential photovoltaic absorbers based on first-principles spectroscopic screening of materials. *Phys. Rev. Lett.* **2012**, *108*, 068701. [CrossRef]